Scanning Electron Microscopy

Volume 1982
Number 1 *1982*

Article 25

1982

Backscattered Electron (BSE) Imaging in the Scanning Electron Microscope (SEM) - Measurement of Surface Layer Mass-Thickness

Oliver C. Wells
IBM Thomas J. Watson Research Center

Richard J. Savoy
IBM Thomas J. Watson Research Center

Phillip J. Bailey
IBM Thomas J. Watson Research Center

Electron Beam Interactions With Solids (Pp. 287-298)
SEM, Inc., AMF O'Hare (Chicago), IL 60666, U.S.A.

BACKSCATTERED ELECTRON (BSE) IMAGING IN THE SCANNING ELECTRON MICROSCOPE (SEM) – MEASUREMENT OF SURFACE LAYER MASS-THICKNESS

Oliver C. Wells, Richard J. Savoy and Phillip J. Bailey
IBM Thomas J. Watson Research Center
P.O. Box 218, Yorktown Heights, NY 10598
Phone No. (914) 945-2321

ABSTRACT

Sometimes, the sample to be examined in the SEM will consist of a compositionally non-uniform substrate that is covered by an approximately uniform surface layer. With a low enough incident beam energy, only the surface layer can be seen in the SEM image. The underlying structure can be seen in the secondary electron (SE) image if the range of the incident electrons is greater than twice the thickness of the surface film. In the backscattered electron (BSE) image the threshold energy is higher because the BSE detector is insensitive to slow electrons. The information depth in the BSE image was investigated experimentally as a function of incident energy and BSE detector position using test specimens in which an Al layer of thickness either 210 or 1,100 nm was deposited onto an aluminised Si wafer covered by a pattern of gold lines. It was estimated that a lower limit to the surface mass-thickness that can be measured using a solid-state BSE detector is $\sim 10 \mu g/cm^2$ ($=40$ nm of Al) for the BSE method, as compared with $\sim 0.25 \mu g/cm^2$ ($=1$ nm of Al) for the low-loss electron method. There would seem to be no reason why measurements by the BSE method could not be carried out automatically in a computer-controlled SEM equipped with image analysis and using the standard BSE detector systems, to measure the mass-thickness of a surface layer.

Keywords: Backscattered electron image, Electron penetration, Image contrast in scanning electron microscopy, Information depth, Mass-thickness of surface layer, Multi-layered sample, Secondary electron image, Angular distribution of backscattered electrons.

1. INTRODUCTION

The idea which runs through this paper is the way in which both the secondary electron (SE) image and the backscattered electron (BSE) image of a solid specimen in the scanning electron microscope (SEM) are affected by BSE from the deeper layers. The samples consist of an approximately uniform surface layer over a substrate in which the atomic number Z is non-uniform. A question of some interest is how to measure the mass-thickness of such a surface layer in terms of the beam energy at which the underlying structure becomes visible in the recorded image. A second question is whether such measurements would be feasible on a routine basis with an automated SEM.

In the SE image, the collected current arises jointly from SE that are excited as the primary electrons *enter* the specimen, by SE excited at the surface of the specimen by re-emerging BSE, by SE that are excited by the BSE from the surrounding objects in the specimen chamber, and by BSE that enter the detector directly. It is the last three of these that are affected by the structure that lies below the surface. The practical importance of this can be seen from the following examples from SEM service work. Fig. 1 shows an oxidised silicon wafer on which there had been deposited 0.19 μm of Cr, 0.13 μm of Si, and 0.15 μm of Au. This had been heated to 300° C in He so that intermixing and segregation effects have occurred between the Si and Au layers. It was required to discover whether a surface layer of any kind had been formed over these high-Z and low-Z segregated regions.

SE images obtained in a Hitachi S-450-LB SEM at beam energies of 3, 4, and 10 keV are shown in Figs. 1(a)-(c). The detector was of the type described by Everhart and Thornley (1960). The differences between these images are very striking. With the lowest beam energy, only the surface topography can be seen. As the beam energy is increased, the surface topography fades away, and the image contrast caused by the underlying structure becomes dominant. This effect is caused by a surface layer (actually of SiO_2) which lies over the segregated regions. In addition, the dust particles which are so evident at 3 keV can hardly be seen at 10 keV. A similar sample had been fractured and examined in cross-section by Wells and Aliotta (1979), and a low density surface layer of thickness 100 nm had been found.

Examination of Figs. 1(a) and 1(b) shows that the underlying structure is just beginning to become visible as the incident beam energy is raised from 3 keV to 4 keV. It is there-

LIST OF SYMBOLS

AB + BC	= Path length as defined in Fig. 11 (in nm).
BSE	= Backscattered electron.
C_{BA}	= Image contrast as defined in Eq. 5 (dimensionless).
D	= Film thickness as shown in Fig. 6 (in nm).
E	= Incident electron energy (in keV).
E_{th}	= Threshold energy of BSE detector (in keV).
$E_{1.0}$, $E_{1.1}$ and $E_{1.2}$	= Intercepts of the best-fitting straight lines in Figs. 9 and 10 with $\eta_B/\eta_A =$ 1.0, 1.1 and 1.2 (in keV).
EB	= Electron beam.
R	= Electron range as given by Eqs. 1 or 2 (in mg/cm² in the general case, or in nm of Al if so stated).
R_{th}	= Electron range in the specimen for an electron of energy E_{th} (in nm).
$R_{1.0}$, $R_{1.1}$ and $R_{1.2}$	= Electron ranges in the specimen corresponding to $E_{1.0}$, $E_{1.1}$ and $E_{1.2}$ (in nm).
SEM	= Scanning electron microscope.
SE	= Secondary electron.
Z	= Atomic number,
δ_A, δ_B	= Secondary emission coefficients that correspond to η_A, η_B.
η_A, η_B	= BSE coefficients of the regions shown in Fig. 6 as weighted for the energy sensitivity of the BSE detector.
θ_1	= Glancing angle of incidence (Figs. 4 and 6).
θ_2	= Takeoff angle of BSE detector (Figs. 4 and 6).

fore to be expected that the extrapolated electron range will be approximately twice the thickness of the surface SiO_2 layer over that energy range. From Eq. 1 below, the range of 4 keV electrons is 0.07 mg/cm². If the density of SiO_2 is 2.66 gm/cm³, then this corresponds to 260 nm, which is ~2.6 times greater than the 100 nm surface layer seen in the cross-sectioned sample. (To obtain the exact ratio of 2:1 it is necessary to assume an incident energy of 3.3 keV. This point is discussed below.) Extrapolation from the data of Gentsch and Reimer (1973; their Fig. 2) suggests that a 10 keV electron beam is broadened by ~50 nm following penetration through 100 nm of SiO_2. This is consistent with the observed sharpness of the image of the underlying structure shown in Fig. 1(c).

A second example is shown in Fig. 2. This is a thin-film recording head in which the pole-tip regions are covered by a thin surface layer. SE images obtained using a Cambridge S250 at energies of 5.1, 10 and 30 keV are shown in Fig. 2. At 5.1 keV, only the surface topography can be seen (Fig. 2a). At 10 keV, the BSE from the buried pole-tips give rise to SE which are then collected, and this shows both the positions and some surface structure of these regions (Fig. 2b). At 30 keV, the image is similar, except that the resolution is now degraded by the increased electron penetration in the target (Fig. 2c). When examining this sample, therefore, there is a critical energy at which the surface of the pole-tips can be seen most clearly.

Comparison pairs of SE images in which the underlying structure becomes visible as the beam energy is raised have also been published by Beaufrere (1974) and by Wolf (1974).

ELECTRON BACKSCATTERING FROM MULTI-LAYER TARGETS

Niedrig (1978 and 1982) has reviewed electron backscattering from thin-film and multi-layer targets. Only selected topics are considered here.

Electron backscattering from multi-layer targets (and with normal electron incidence) was investigated by Holliday and Sternglass (1955, 1957, 1959). Thin films of different materials and thicknesses were deposited onto substrates of substantially different Z. Electrons having an energy greater than 50 eV were collected over a large solid angle and were measured as a function of the incident energy. The range of electrons in the surface film for a particular beam energy was then defined as being twice the thickness of the film for which the backscattering coefficient was affected by the underlying substrate.

The values of electron range R cited below were taken from the best-fitting straight line to the curve published by Holliday and Sternglass (1959 their Fig. 5), and Kanter 1961 (his Fig. 5), for the energy range from ~1.5 to ~16 keV:

$$R = 0.01 \times E^{1.40}\ \text{mg/cm}^2 \qquad 1$$

or:

$$R = 37 \times E^{1.40}\ \text{nm for Al} \qquad 2$$

where E is in keV. For energies greater than ~10 keV, the curve becomes steeper, and a more accurate relation was given by Everhart and Hoff (1971):

$$R = 0.004 \times E^{1.75}\ \text{mg/cm}^2 \qquad 3$$

or:

$$R = 17 \times E^{1.75}\ \text{nm for Al} \qquad 4$$

where E is in keV. (The energy for which Eq. 1 and Eq. 3 give the same answer of R = 0.390 mg/cm² is E = 13.7 keV.)

BSE IMAGE IN THE SEM

In the SEM, the specimen can be mounted either at right angles or at an oblique angle to the incident electron beam. BSE have been detected in the SEM in the following ways:

(1) By collecting the SE from a suitably placed surface (McMullan 1953, Moll et al. 1978, Reimer and Volbert 1979).

(2) With a grounded scintillator or phosphor screen which subtends a large solid angle at the specimen surface (Smith 1956; Cosslett and Duncumb 1957; Wells 1957, 1970 and 1979; Everhart, Wells and Oatley 1959; Blaschke 1970; Schur, Blaschke and Pfefferkorn 1973 and 1974; Robinson 1974), or with a small solid angle (Everhart and Thornley 1960).

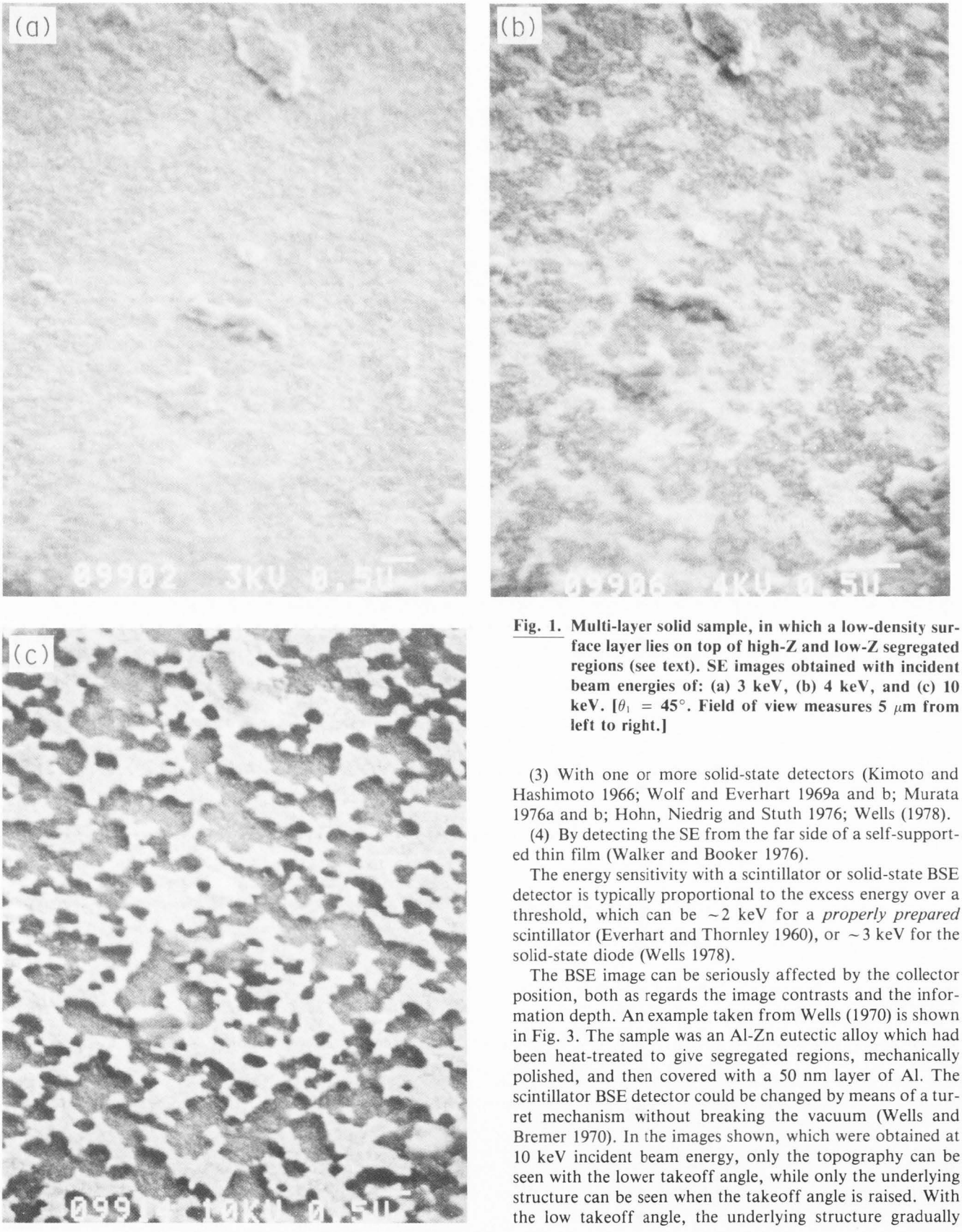

Fig. 1. Multi-layer solid sample, in which a low-density surface layer lies on top of high-Z and low-Z segregated regions (see text). SE images obtained with incident beam energies of: (a) 3 keV, (b) 4 keV, and (c) 10 keV. [$\theta_1 = 45°$. Field of view measures 5 μm from left to right.]

(3) With one or more solid-state detectors (Kimoto and Hashimoto 1966; Wolf and Everhart 1969a and b; Murata 1976a and b; Hohn, Niedrig and Stuth 1976; Wells (1978).

(4) By detecting the SE from the far side of a self-supported thin film (Walker and Booker 1976).

The energy sensitivity with a scintillator or solid-state BSE detector is typically proportional to the excess energy over a threshold, which can be ~2 keV for a *properly prepared* scintillator (Everhart and Thornley 1960), or ~3 keV for the solid-state diode (Wells 1978).

The BSE image can be seriously affected by the collector position, both as regards the image contrasts and the information depth. An example taken from Wells (1970) is shown in Fig. 3. The sample was an Al-Zn eutectic alloy which had been heat-treated to give segregated regions, mechanically polished, and then covered with a 50 nm layer of Al. The scintillator BSE detector could be changed by means of a turret mechanism without breaking the vacuum (Wells and Bremer 1970). In the images shown, which were obtained at 10 keV incident beam energy, only the topography can be seen with the lower takeoff angle, while only the underlying structure can be seen when the takeoff angle is raised. With the low takeoff angle, the underlying structure gradually

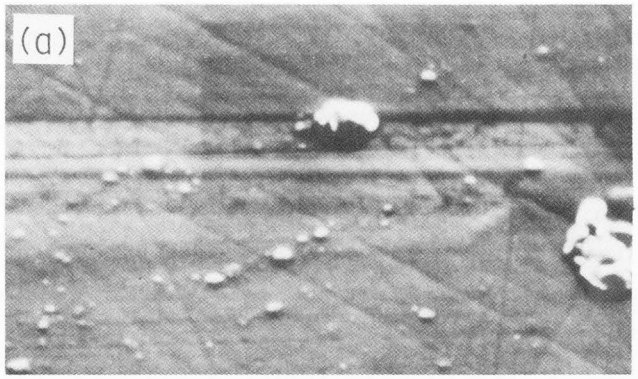

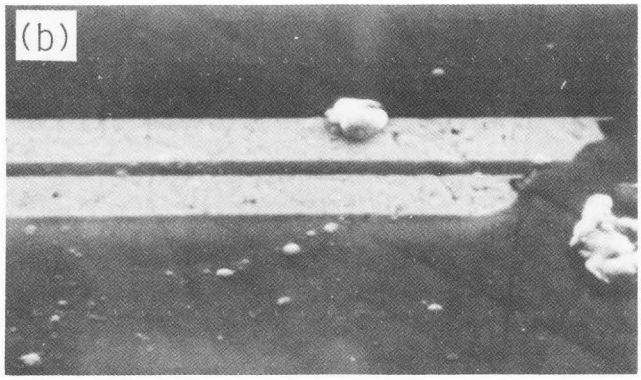

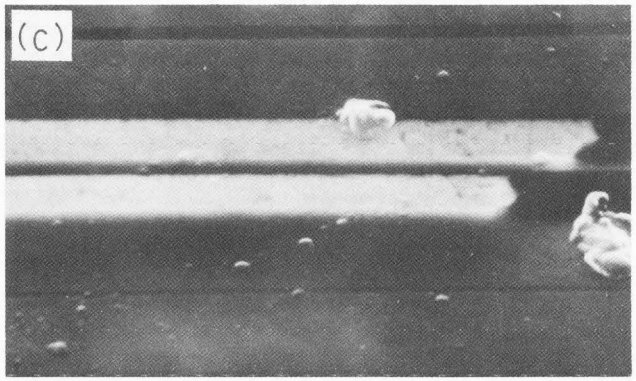

Fig. 2. Pole-tip regions of thin-film magnetic recording head. SE images obtained with incident beam energies of: (a) 5.1 keV, (b) 10 keV, and (c) 30 keV. [θ_1 = 45°. Field of view measures 15 μm from left to right.]

becomes visible as the beam energy is raised from 10 to 15 keV. This is a case when the information depth is affected by both the incident electron energy and by the detector position.

Extensive studies of the escape depth in the BSE image have been published by Murata (1971 through 1976). A self-supported thin copper film was placed across a hold in a copper target, and the image contrast was measured as a function of the film thickness, the incident beam energy and the detector position. The experimental results were compared with Monte Carlo calculations. Hohn, Niedrig and Stuth (1976) measured BSE from a self-supported film target using a moveable solid-state detector. Hohn, Kindt, Niedrig and Stuth (1976) measured BSE from multi-layer targets, and discussed the information depth. Seiler (1976) measured the information depth in the SE image for a Cu film over a substrate consisting of Ag, Al, Au and Fe. (His measurements, which were made for a signal-to-background ratio of 0.01 in the recorded SE image, can be expected to be slightly smaller than measurements made by extrapolation of the curves obtained here.)

The corresponding results for the information depth in the low-loss image are as follows (Wells 1971). The sample shown in Fig. 3 was cleaned, and then recoated with an Al layer of thickness 11 nm. With 15 keV primary energy, the underlying structure became visible in the image formed by BSE with less than 800 eV energy loss. Since a low-loss image with a loss of 100 eV or less is perfectly practical, this shows that Al surface layers of thicknesses down to $\sim$1 nm should be measurable by this method. (These low-loss results were obtained using a retarding-field energy filter together with a scintillator-photomultiplier electron detector.)

The BSE detector system that was used in the present work consists of a pair of solar cells that can be moved round the specimen to vary the takeoff angle (Fig. 4). These were type 55CL (Optical Coating Lab. Inc., City of Industry, CA 91746). Each solar cell subtends a cone measuring 22° by 22° at the surface of the specimen, and provides a current gain proportional to the excess energy above $\approx$3 keV (Fig. 5). (In this work, only one of the solar cells was used.)

Speaking in general terms, the effect of the collector takeoff angle θ_2 (as defined in Fig. 4) on the BSE image can be summarised as follows:

(1) Topographic contrast can be minimised by the use of a high takeoff angle. Thus, with normal electron incidence, topographic contrast can be minimised by arranging the BSE detector symmetrically about the beam (see, for example McMullan 1953; his Fig. 4). With an inclined sample, a critical detector position exists in the neighborhood of $\theta_2 = 90°$ when topography in the form of surface waves (but *not* in the form of small holes) is minimised (Fathers et al. 1973 and 1974; Schur, Blaschke and Pfefferkorn 1974). This can be achieved, for a fixed detector position, by adjusting the tilt angle of the specimen until the collected BSE current is a maximum. For a magnetised sample, type-2 magnetic contrast is usually close to the optimum with the detector in this position (Fathers 1973 and 1974; Wells 1978).

(2) Topographic contrast from small features on an otherwise flat surface can be enhanced by the use of a takeoff angle θ_2 less than $\sim 20°$.

(3) In general, the information depth can be reduced by using a small value of θ_2.

(4) If both θ_1 and θ_2 are small enough, then contrast reversal can occur, so that the heavier material is less bright in the BSE image (Wells 1970 for precipitates in a Cu-Al alloy; Reimer, Popper and Bröcker 1978 for more detailed studies, including the voltage-sensitive nature of this effect). This effect is discussed in connection with an Al and Au sample below.

EXPERIMENTAL RESULTS

Experiments were made to determine the information depth in the BSE image as a function of the incident beam

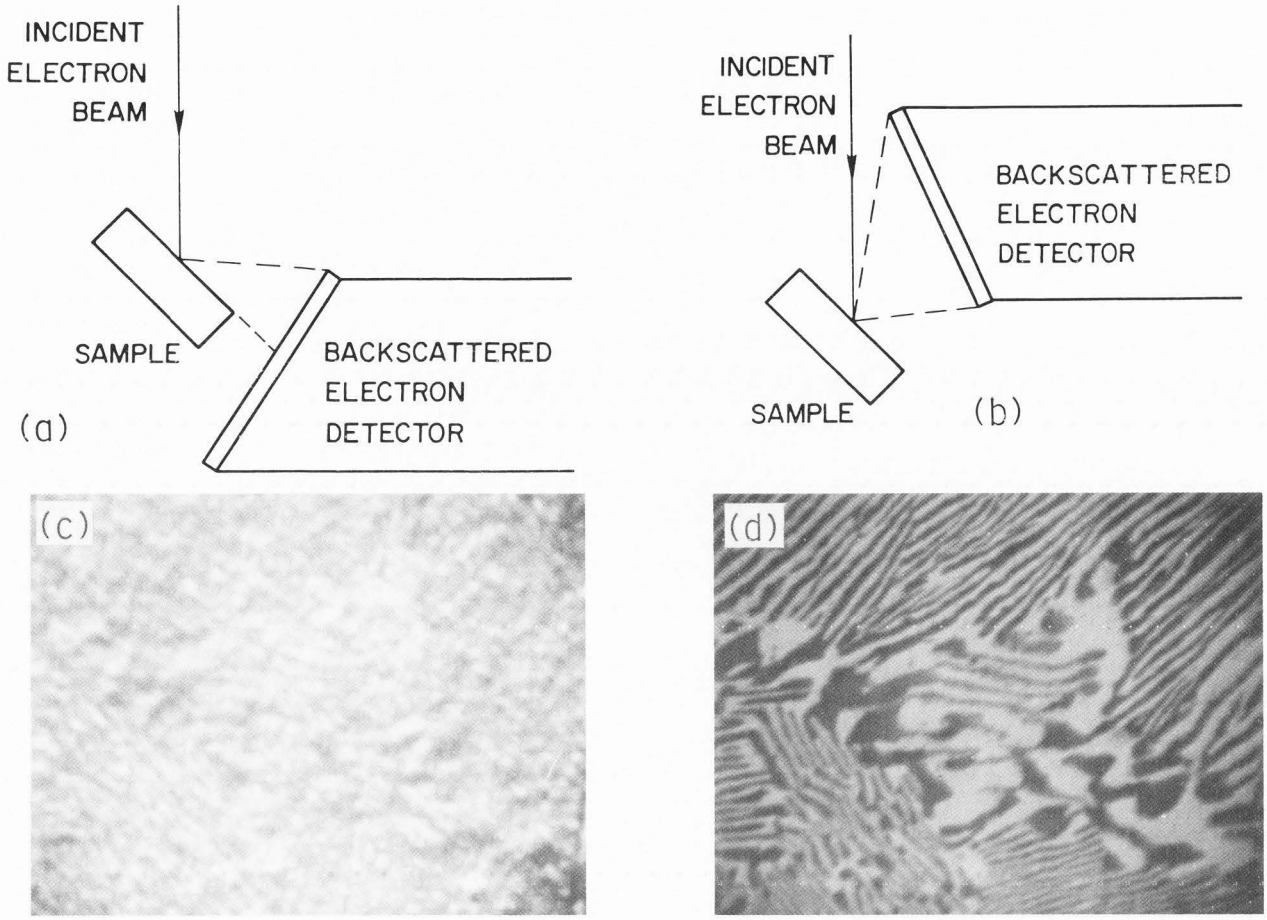

Fig. 3. Al-Zn eutectic alloy heat treated to give segregated regions, mechanically polished, and covered with 50 nm of Al. (a) Scintillator BSE detector with low take-off angle. (b) BSE detector with high takeoff angle. (c, d) BSE images obtained with detectors shown above. [$\theta_1 = 45°$. Field of view measures 15 μm from left to right. From Wells 1970.]

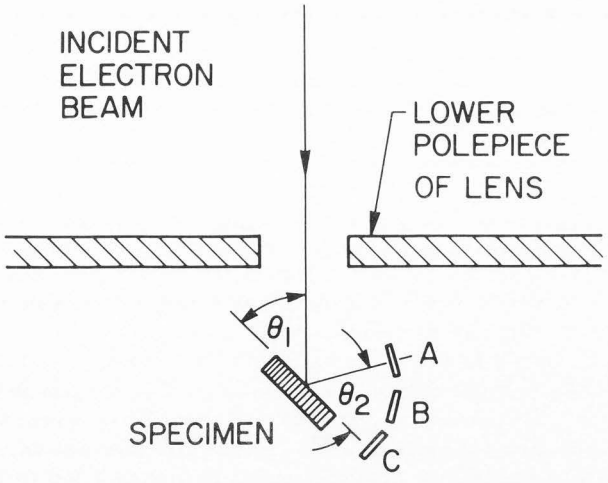

Fig. 4. Movement of solid-state BSE detectors around the sample (from Wells 1978).

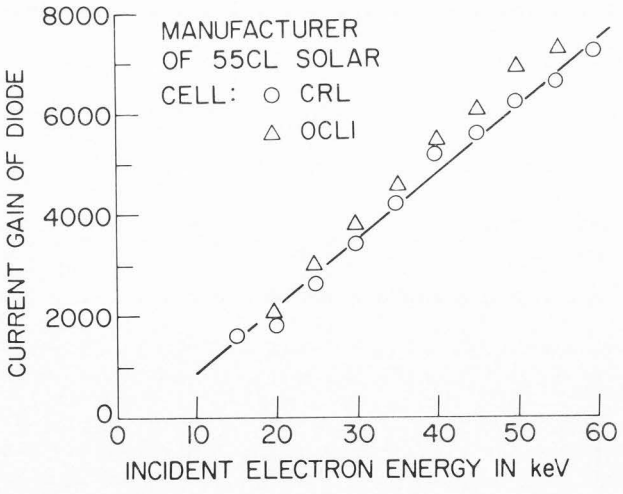

Fig. 5. Energy sensitivity of solid-state BSE detector (from Wells 1978).

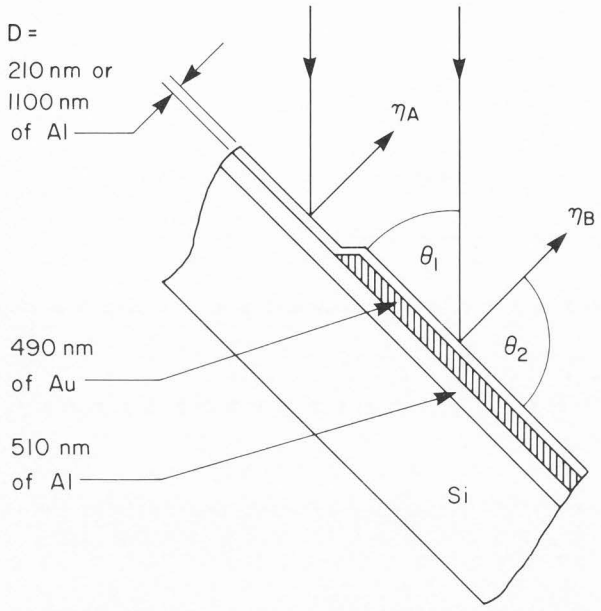

Fig. 6. Sample used in present work. Definitions of θ_1 and θ_2. See text for definitions of η_A and η_B.

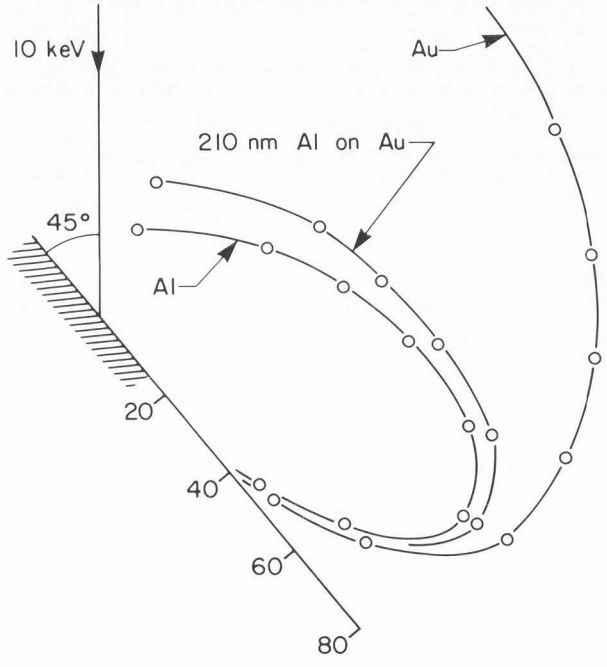

Fig. 7. Angular distribution of BSE from: "Al," "Al-on-Au," and "Au" (as defined in text). [θ_1 = 45°. Incident beam energy = 10 keV.]

energy and collector takeoff angle. Samples were prepared as follows (Fig. 6). A 0.51 μm layer of aluminum was EB-evaporated onto a silicon wafer from which the oxide had been removed. A 0.49 μm gold layer was then EB-evaporated through a mask. On one wafer, a further 210 nm aluminum layer was evaporated over the entire surface (Fig. 6). On a different wafer, the thickness of this final Al layer was 1100 nm. The deposition rates were measured with a crystal rate monitor (3 nm/sec for Al, 1.5 nm/sec for Au). The pressure during evaporation was 1.4×10^{-6} Torr for Al, 3.0×10^{-6} Torr for Au. All evaporations were carried out with the substrate at room temperature. The resulting film thicknesses were confirmed by a mechanical step measurement.

In the following description, the word "Al" refers to 0.51 μm of Al deposited on a cleaned Si wafer; the word "Au" refers to 0.49 μm of gold on top of that; and the expression "Al-on-Au" refers to either 210 or 1100 nm of Al deposited over the Au layer (Fig. 6). The quantities η_A and η_B shown in Fig. 6 are the BSE coefficients as weighted for the energy sensitivity of the BSE detector. (In fact it was the output current of the detector that was measured as a multiple of the current onto the sample. No attempt was made to measure either η_A or η_B absolutely.)

Angular distribution curves for "Al", "Al-on-Au" (with 210 nm of Al), and "Au" are shown in Fig. 7. The incident beam energy was 10 keV, and the glancing angle of incidence θ_1 was 45°. At the peak of the "Al" curve, the current from the diode was 70 times greater than the incident beam current. If the beam energy is increased, then the angular distribution curve for "Al-on-Au" moves away from the "Al" curve and closer to the "Au" curve.

The most striking characteristic of the "Al" and "Au" curves is that for large values of θ_2 (that is, for the collector closer to the beam), there is a strong compositional contrast. For $\theta_2 < \sim 20°$, these two curves lie closely together, which indicates that compositional image contrast is minimised for a low takeoff angle. (Topographic contrasts are strongest with the collector in this position, so that the compositional contrasts may be concealed by them.)

Fig. 8 shows BSE images of a Au stripe of thickness 490 nm (and with *no* Al overlayer) on an aluminised Si wafer. The glancing angle of incidence $\theta_1 = 30°$ in all cases. Figs. 8(a) thru (c) were obtained with a beam energy of 6 keV, while the energy was 10 keV for the remainder. With the high takeoff angle ($\theta_2 = 110°$), the center Au region appears brighter in both cases (Figs. 8c and f). At 10 keV, the Au region is brighter than the Al for all values of θ_2. But at 6 keV, the Au and Al are equally bright for $\theta_2 = 50°$ (Fig. 8b), and the contrast is reversed for a lower takeoff angle than this (Fig. 8a). It is not easy to see how a voltage-sensitive contrast reversal of this kind can be predicted by a Monte Carlo calculation based on the Rutherford scattering cross-section for the wide-angle events, because such calculations generally give results that can be scaled on the beam energy. Reimer (personal communication) has pointed out that the Mott scattering cross-section, which is different from the Rutherford at electron energies less than ~10 keV, might provide a possible explanation for these effects. In any event, it would appear that these contrast reversal effects provide one way in which Monte-Carlo calculations based on the Mott theory and the Rutherford theory can be compared.

To obtain data for the escape depth, the ratio η_B/η_A of the "Al-on-Au" and "Al" detected currents for fixed incident and takeoff angles were measured as a function of the primary beam energy (Figs. 9 and 10). The beam voltage was measured with a digital voltmeter operating from a 1,000 to 1 voltage divider (Fluke Model 80K-40 HV Probe). The video

signal was measured with a second digital voltmeter as the beam was scanned at (effectively) television speed in a reduced-area raster. This raster was moved back and forth across the edge of the underlying gold layer. For each experimental setting, the average was taken of twelve values of η_B/η_A as measured in this way. This ratio was plotted as a function of incident beam energy for different values of the takeoff angle (Figs. 9 and 10).

Similar (but considerably less extensive) measurements of the ratio between the corresponding secondary emission coefficients δ_B and δ_A were plotted as a function of the beam energy, and gave an intercept energy of ~5 keV. This is in substantial agreement with measurements from an Al film of very nearly 210 nm thickness over an Au substrate made by Holliday and Sternglass (1957; their Fig. 4). (The advantage of the BSE method lies in the possibility of eliminating topographic contrast.)

DISCUSSION

It is clear that the ratio η_B/η_A will be unity for a low enough incident beam energy, and that it will increase in some manner if the energy exceeds a "threshold" value which must now be defined in some way. Holliday and Sternglass (1957 and 1959) plotted the absolute values of the unweighted BSE coefficient η, and this is probably best as far as studying the process is concerned. Easier options are, however, to measure either the ratio η_B/η_A or the *image contrast* C_{BA} defined as:

$$C_{BA} = \frac{\eta_B - \eta_A}{\eta_B + \eta_A} \qquad 5$$

The two quantities η_B/η_A and C_{BA} are plotted as a function of incident electron energy in Fig. 9. If $\eta_B/\eta_A < \sim 1.2$, then there is very little to choose between the values that are obtained. But if $\eta_B/\eta_A > \sim 1.2$, then the curve for η_B/η_A is found to be essentially straight over a greater range of incident energy. This makes it easier to determine the point at which the extrapolated curve meets the zero-contrast axis. In these studies, the curves obtained by plotting η_B/η_A were used.

Fig. 10 shows the dependence of the ratio η_B/η_A on the incident electron energy of $\theta_2 = 110°$, 45°, 21°, and 9° for the two values of Al film thickness D = 210 nm (Fig. 10a) and D = 1100 nm (Fig. 10b). The extrapolated intercept $E_{1.0}$ of these curves with the line where $\eta_B/\eta_A = 1$ does not change too greatly as θ_2 is changed. What *does* change, however, is energy intercept of these curves with the larger values of the ratio η_B/η_A.

Numerical data in Table 1 for 210 nm of Al, and in Table 2 for 1100 nm of Al on the specimen shown in Fig. 6. The rows in these tables are as follows:

Path length AB + BC. Everhart (1960) described an electron backscattering model for normal electron incidence in which the incident electrons are assumed to travel in straight lines except for a single wide-angle scattering event. This was modified for oblique incidence by Shimizu and Shinoda (1963). The *path length* AB + BC as defined in Fig. 11 is the shortest distance that a BSE must travel if it is to reach the surface according to this model. The electron ranges as calculated from the energy intercepts are normalised relative to AB + BC in rows 9-11 in Tables 1 and 2.

Threshold energies. The three energies $E_{1.0}$, $E_{1.1}$ and $E_{1.2}$ shown in rows 3-5 are defined as the intercepts of the best-fitting straight lines in Figs. 9 and 10 with η_B/η_A = 1.0, 1.1 and 1.2.

Electron range. The three ranges $R_{1.0}$, $R_{1.1}$ and $R_{1.2}$ shown in rows 6-8 were calculated from Eq. 1 or Eq. 3 to correspond with $E_{1.0}$, $E_{1.1}$ and $E_{1.2}$. These are expressed as a multiple of the appropriate value of AB + BC in rows 9-11. For θ_2 greater than 30°, the ratio $R_{1.0}/AB + BC$ is within 10% of unity, indicating that $R_{1.0}$ is a useful estimate of the film thickness in that case.

A correction should be made to $R_{1.0}$ by subtracting the range R_{th} corresponding to the energy threshold E_{th} of the BSE detector. Thus, if E_{th} = 3 keV, then (from Eq. 1), R_{th} = 0.047 mg/cm² (= 170 nm for Al).

Information depth. Intuitively, it would appear from Fig. 3 that the information depth should be significantly increased if the takeoff angle is raised. The comparatively minor variations in $E_{1.0}$ with θ_2 shown in Figs. 9 and 10 and in Tables 1 and 2 may therefore come as a surprise. However, the variations in $E_{1.1}$ and $E_{1.2}$ with θ_2 are considerably greater, which shows that the depth to give a specified contribution to the image contrast varies more rapidly with the takeoff angle than does the thickness as estimated from $E_{1.0}$.

CONCLUSIONS

The main conclusion from this work is that the BSE method for measuring the mass-thickness of a surface layer on a solid target is ready to be more widely applied (using the standard BSE detector systems) by means of automated techniques.

A lower limit to the surface mass-thickness that can be measured is imposed by the need to have the incident beam energy greater than the energy threshold E_{th} of the BSE detector by an amount that is large enough to give a measurable signal. Since the sensitivity of a solid-state detector increases gradually from zero above E_{th}, it might be expected that the BSE detector will become adequately sensitive for BSE having an energy of several times E_{th}. As a first approximation, it might therefore be expected that the smallest measurable film thickness will be of the same order of magnitude as the range R_{th}. Thus, if a solid-state BSE detector can be found with a threshold energy of 1 keV, then a lower thickness limit of ~10 μg/cm² (=40 nm of Al) might be expected. The possibility of using a converter-type BSE detector with its improved low energy response must also be considered. In the low-loss image, the energy threshold of the detector is precisely defined by a retarding-field energy filter, and thicknesses down to 0.25 μg/cm² (= 1 nm of Al) can be measured by adjusting this cut-off energy relative to the incident beam energy.

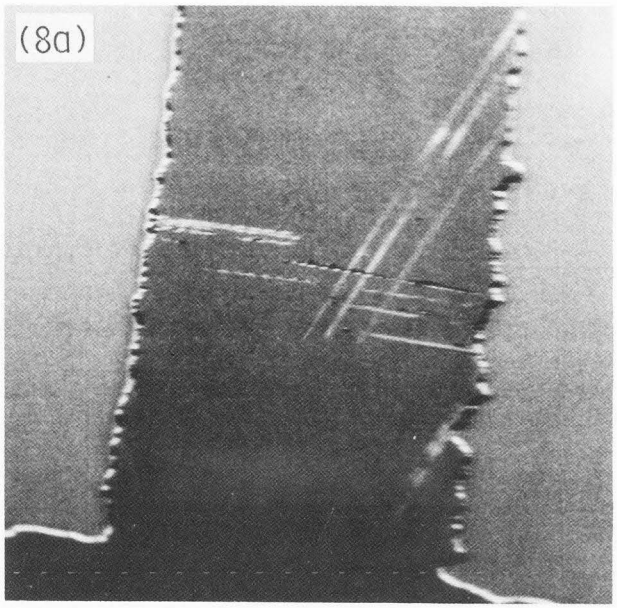
(8a)

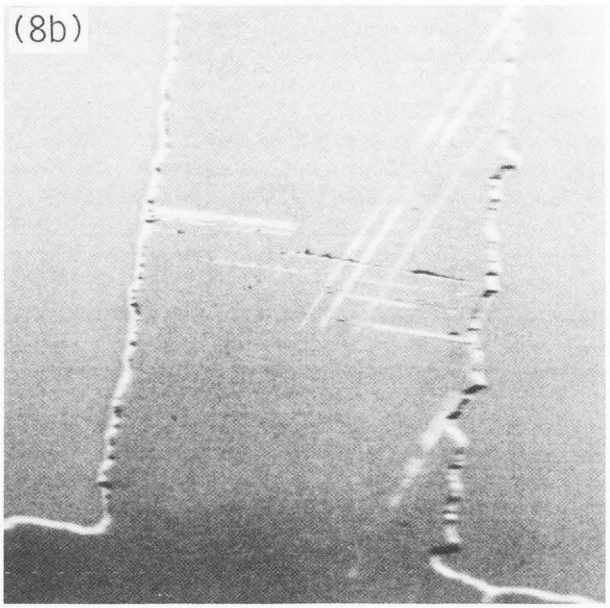
(8b)

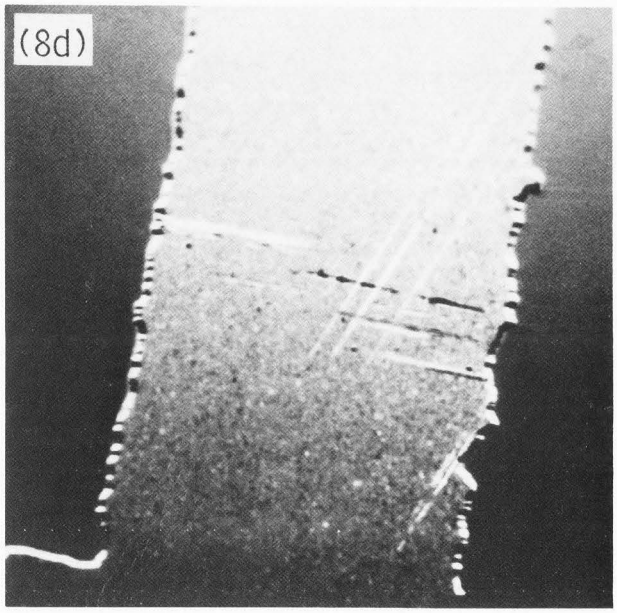
(8d)

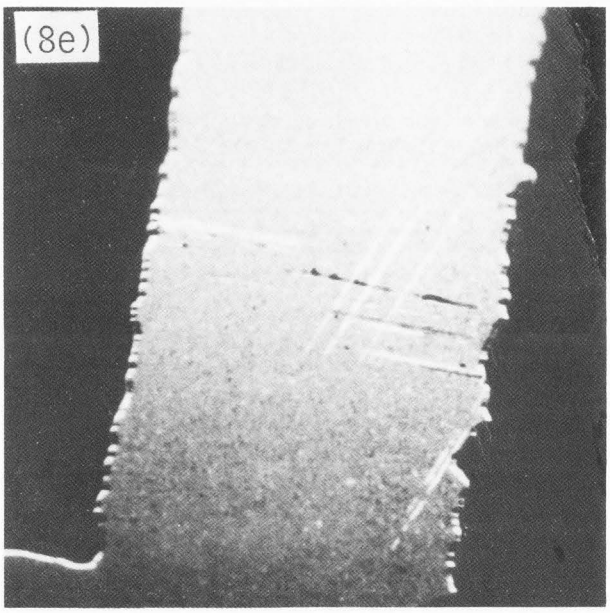
(8e)

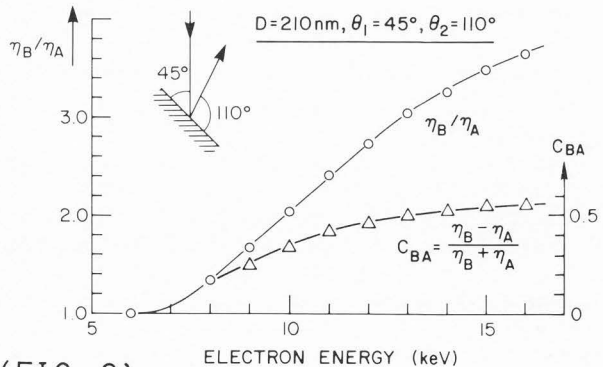
D=210nm, θ1=45°, θ2=110°
45°
110°
ηB/ηA
CBA
CBA = (ηB − ηA)/(ηB + ηA)
3.0
2.0
1.0
0.5
0
5
10
15
ELECTRON ENERGY (keV)

(FIG. 9)

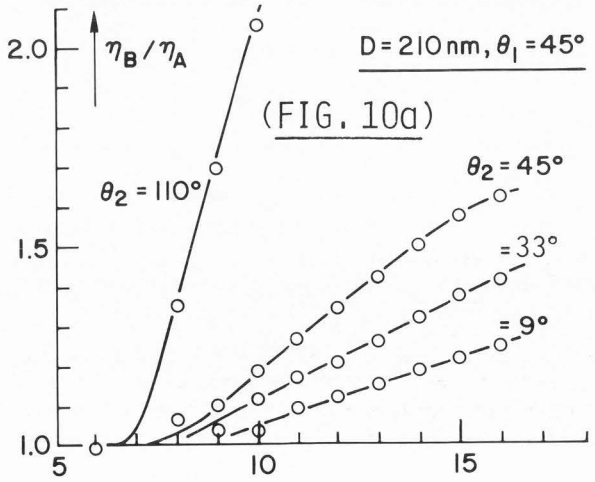
2.0
1.5
1.0
ηB/ηA
D=210nm, θ1=45°
θ2=110°
θ2=45°
=33°
=9°
5
10
15

(FIG. 10a)

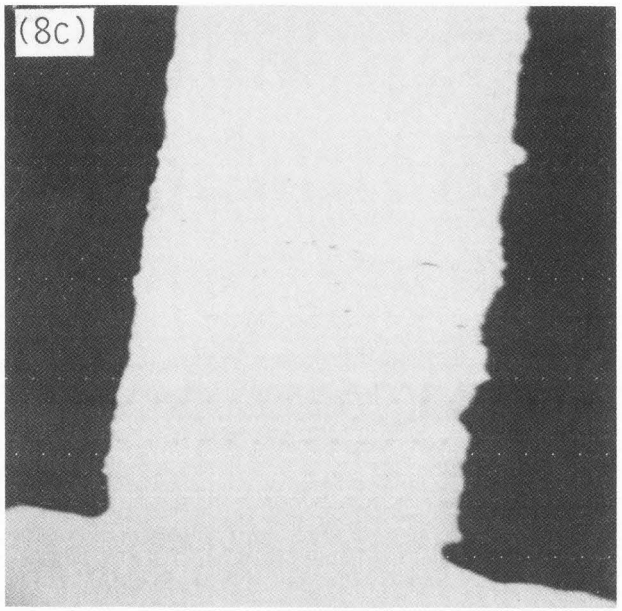

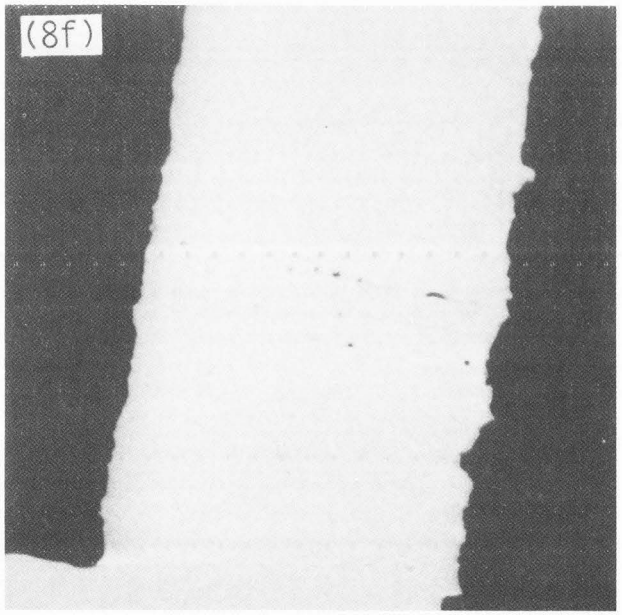

Fig. 8. Sometimes the compositional contrast reverses between Au and Al (see text). Here, $\theta_1 = 30°$ in all images. At 6 keV the contrast reverses: (a) $\theta_2 = 40°$, (b) $\theta_2 = 50°$, (c) $\theta_2 = 110°$. At 10 keV it does not (d as in a, e as in b, f as in c). Field of view measures 180 μm from left to right.

Fig. 9. Ratios η_B/η_A, and $\dfrac{\eta_B - \eta_A}{\eta_B + \eta_A}$ as functions of incident electron energy for $\theta_1 = 45°$, $\theta_2 = 110°$ and D = 210 nm.

Fig. 10. Ratio η_B/η_A as a function of incident electron energy (with $\theta_1 = 45°$) for $\theta_2 = 110°$, 45°, 33°, and 9°: (a) D = 210 nm, and (b) D = 1100 nm.

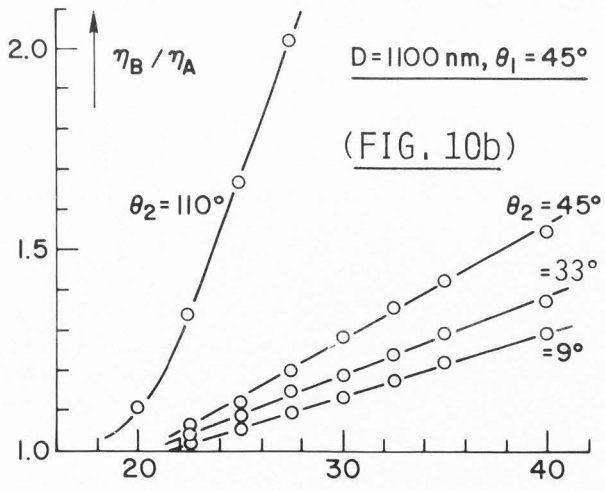

Fig. 11. The "path length" in Table 1 is defined as AB + BC.

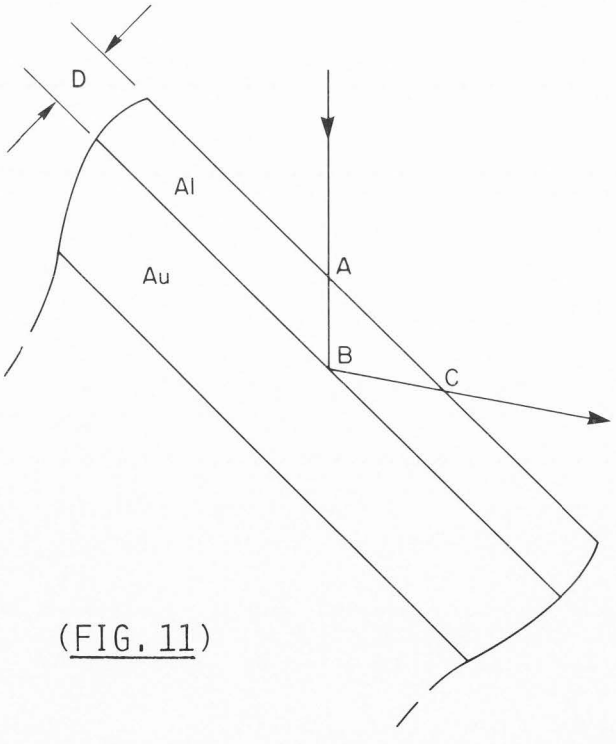

Table 1. Numerical data with D = 210 nm.

				$\theta_1 = 45°$				$\theta_1 = 90°$	
1.	$\theta_2 =$	110°	45°	33°	21°	9°	74°	30°	10°
2.	in nm: AB + BC	520	594	683	8 8 3	1640	428	630	1420
3.	in keV: $E_{1.0}$	6.92	7.63	7.83	7.81	8.38	6.22	7.06	7.45
4.	$E_{1.1}$	7.5	9.0	9.7	11.3	11.3	6.45	7.49	8.00
5.	$E_{1.2}$	8.2	10.1	11.6	14.0	14.2	6.68	7.92	8.55
6.	in nm: $R_{1.0}$	550	636	660	658	726	478	571	615
7.	$R_{1.1}$	621	802	891	1100	1100	503	620	680
8.	$R_{1.2}$	704	942	1140	1490	1520	528	671	746
9.	$\frac{R_{1.0}}{AB + BC}$	1.06	1.07	0.97	0.75	0.44	1.12	0.91	0.43
10.	$\frac{R_{1.1}}{AB + BC}$	1.19	1.35	1.30	1.25	0.67	1.17	0.98	0.48
11.	$\frac{R_{1.2}}{AB + BC}$	1.35	1.59	1.67	1.69	0.93	1.23	1.07	0.53

Table 2. Numerical data with D = 1,100 nm.

				$\theta_1 = 45°$				$\theta_1 = 90°$	
1.	$\theta_2 =$	110°	45°	33°	21°	9°	74°	30°	10°
2.	in nm: AB + BC	2730	3110	3580	4630	8590	2240	3300	7430
3.	in keV: $E_{1.0}$	19.6	20.1	20.0	20.2	20.9	18.7	19.6	19.3
4.	$E_{1.1}$	20.0	23.5	25.3	27.0	27.2	19.2	20.4	20.3
5.	$E_{1.2}$	20.8	27.0	30.5	34.0	33.7	19.7	21.4	21.7
6.	in nm: $R_{1.0}$	2740	2860	2840	2890	3060	2520	2740	2670
7.	$R_{1.1}$	2840	3760	4280	4800	4860	2640	2940	2910
8.	$R_{1.2}$	3040	4800	5940	7180	7070	2760	3190	3270
9.	$\frac{R_{1.0}}{AB + BC}$	1.00	0.92	0.79	0.62	0.36	1.13	0.83	0.36
10.	$\frac{R_{1.1}}{AB + BC}$	1.04	1.21	1.20	1.04	0.57	1.18	0.89	0.39
11.	$\frac{R_{1.2}}{AB + BC}$	1.11	1.54	1.66	1.55	0.82	1.23	0.97	0.44

The measurements described in this paper were very time-consuming, involving the repeated readjustment of instrumental parameters, and a repetitive calculation, averaging and plotting of the ratios. Also, it is not easy to make measurements from an image having irregular areas of different contrast as is the case in Figs. 1 or 3. In a properly automated SEM having an image processing facility, the different regions could be identified from the peaks in the histogram of the gray levels present in the image, after which the curves could be plotted and evaluated automatically. This would therefore add another method for quantitative measurement to existing techniques.

ACKNOWLEDGMENTS

The micrographs shown in Fig. 3 were obtained by C.G. Bremer. We would like to thank D.A. Chance for providing the samples shown in Fig. 1, D.J. Mikalsen and W. Price for preparing the sample shown in Fig. 6, F. Cardone for calculating $E_{1.0}$ from the experimental data, and F.J. Hohn, J.D. Kuptsis, L. Reimer, H. Seiler and W. Reuter for helpful discussions.

REFERENCES

Beaufrere P. (1974). Micrographs of Al-Cu alloy with precipitates published as Figs. 6.17(e) and (f) in: Scanning Electron Microscopy, O.C. Wells, A. Boyde, E. Lifshin and A. Rezanowich, McGraw-Hill, NY, P. 128.

Blaschke R. (1970). Material analysis by SEM, PhEEM and EPMA. Beitr. elektronenmikroskop. Direktabb. Oberfl. (BEDO). **3**, 17-36 (Remy, Münster 1970).

Cosslett VE and Duncumb P. (1957). A scanning microscope with either electron or x-ray recording. Electron Microscopy. Proc. Stockholm Conf., Sept. 1956. Almquist and Wiksells, Uppsala; Academic Press, New York, 12-14.

Everhart TE, Wells OC and Oatley CW. (1959). Factors affecting contrast and resolution in the scanning electron microscope. J. Electron. Control. **7**, 97-111.

Everhart TE. (1960). Simple theory concerning the reflection of electrons from solids. J. Appl. Phys. **31**, 1483-1490.

Everhart TE and Thornley RFM. (1960). Wide-band detector for micro-microampere low-energy electron currents. J. Sci. Instrum. **37**, 246-248.

Everhart TE and Hoff PH. (1971). Determination of kilovolt electron energy dissipation vs. penetration distance in solid materials. J. Appl. Phys. **42**, 5837-5846.

Fathers DJ, Jakubovics JP, Joy DC, Newbury DE, Yakowitz H. (1973 and 1974). A new method of observing magnetic domains by scanning electron microscopy. Phys. Stat. Sol (a). **20**, 535-544 (1973) and **22**, 609-619 (1974).

Gentsch P and Reimer L. (1973). Measurements of the resolution in the scanning transmission electron microscopy of thick objects. (In German with English abstract). Optik **37**, 451-454.

Hohn FJ, Niedrig H and Stuth B. (1976). Film thickness determination with backscattered electrons using semiconductor detectors. Sixth European Congress on Electron Microscopy, **1** (held in Jerusalem 1976. Tal International Publishing Co.), 380-381.

Hohn FJ, Kindt M, Niedrig H and Stuth B. (1976). Electron backscattering by thin top layers on bulk materials. Sixth European Congress on Electron Microscopy, **1** (held in Jerusalem 1976. Tal International Publishing Co.), 383-385.

Holliday JE and Sternglass EJ. (1955). New method for determining the range of low-energy electrons. (Abstract only). Phys. Rev. **100**, 1238-1239(A).

Holliday JE and Sternglass EJ. (1957). Backscattering of 5-20 keV electrons from insulators and metals. J. Appl. Phys. **28**, 1189-1193.

Holliday JE and Sternglass EJ. (1959). New method for range measurements of low-energy electrons in solids. J. Appl. Phys. **30**, 1428-1431.

Kanter H. (1961). Electron scattering by thin foils for energies below 10 keV. Phys. Rev. **121**, 461-471.

Kimoto S and Hashimoto H. (1966). Stereoscopic observation in scanning microscopy using multiple detectors. The Electron Microprobe. Proc. Symp. held in Washington, D.C., Oct. 1964. T.D. McKinley, K.F.J. Heinrich and D.B. Wittry (eds.), J. Wiley and Sons, New York, U.S.A., 480-489.

McMullan D. (1953). An improved scanning electron microscope for opaque specimens. Proc. IEE. **100** (Pt. II), Inst. Electrical Engineers, London, 245-259.

Moll SH, Healey F, Sullivan B and Johnson W. (1978). A high efficiency, nondirectional backscattered electron detection mode for SEM, Scanning Electron Microsc. 1978; I: 303-310.

Murata K, Matsukawa T and Shimizu R. (1971). Study of the resolution of the backscattered electron image by the Monte Carlo method. Japan. J. Appl. Phys. **10**, 1290-1291.

Murata K. (1973). Monte Carlo calculations on electron scattering and secondary electron production in the SEM, Scanning Electron Microsc. 1973; 267-275.

Murata K. (1976a). Exit angle dependence of penetration depth of backscattered electrons in the scanning electron microscope. Phys. Stat. Sol. (a) **36**, 197-208.

Murata K. (1976b). Depth resolution of the low- and high-deflection backscattered electron images in the scanning electron microscope. Phys. Stat. Sol. (a) **36**, 527-532.

Niedrig H. (1978). Backscattered electrons as a tool for film thickness determination, Scanning Electron Microsc., 1978; I: 841-858.

Niedrig H. (1982). Electron backscattering from thin films. Appl. Phys. Rev. R15-R49 (published as a section in J. Appl. Phys. **53** (4), April 1982).

Reimer L, Popper W and Bröcker W. (1978). Experiments with a small solid angle detector for BSE, Scanning Electron Microsc., 1978; I: 705-710.

Reimer L and Volbert B. (1979). Detector system for backscattered electrons by conversion to secondary electrons. Scanning, **2**, 238-248.

Robinson VNE. (1974). The construction and uses of an efficient backscattered electron detector for SEM. J. Phys. E: Sci. Instrum. **2**, 650-652.

Schur K, Blaschke R and Pfefferkorn G. (1973). Improvement of material and orientation contrasts in the BE-mode of SEM operation using a modified scintillator detector. Beitr. elektronen-mikroskop. Direktabb. Oberfl. (BEDO). **6**, 181-204 (Remy, Münster 1973).

Schur K, Blaschke R and Pfefferkorn G. (1974). Improved conditions for backscattered electron SEM micrographs of polished sections using a modified scintillator detector, Scanning Electron Microsc. 1974, 1003-1010.

Seiler H. (1976). Determination of the "information depth" in the SEM, Scanning Electron Microsc. 1976; I: 9-16.

Shimizu R and Shinoda G. (1963). Scattering of electrons from a microanalyser target. X-Ray Optics and X-Ray Microanalysis, 419-430 (Third Int. Symp. Stanford Univ., Stanford, CA. E.H. Pattee, V.E. Cosslett and A. Engström (Eds.), Academic Press, N.Y.)

Smith KCA. (1956). The scanning electron microscope and its fields of application. Ph.D. Diss., Cambridge Univ., Cambridge, England.

Walker AR, Booker GR. (1976). A simple energy filtering backscattered electron detector. 121-122 in: Developments in Electron Microscopy and Analysis. Proc. EMAG 75 held in Bristol, England, Sept. 1975, J.A. Venables (ed.), Academic Press.

Wells OC. (1957). The construction of a scanning electron microscope and its application to the study of fibres. Ph.D. Diss., Cambridge Univ., Cambridge, England.

Wells OC. (1970). New contrast mechanism for scanning electron microscope. Appl. Phys. Lett. **16**, 151-153. (In Fig. 1, the words "plural scattering" should be replaced by "low takeoff angle" and "multiple scattering" by "high takeoff angle".)

Wells OC and Bremer CG. (1970). Collector turret for scanning electron microscope. Rev. Sci. Instrum., **41**, 1034-1037.

Wells OC. (1971). Low-loss image for scanning electron microscope. Appl. Phys. Lett., **19**, 232-235.

Wells OC. (1978). Effect of collector position on type-2 magnetic contrast in the SEM, Scanning Electron Microsc. 1978; I: 293-298.

Wells OC. (1979). Effects of collector takeoff angle and energy filtering on the BSE image in the SEM. Scanning, **2**, 199-216.

Wells OC and Aliotta CF. (1979). Studies of contamination buildup in the SEM using the BSE imaging technique. Scanning, **2**, 257-259. (The correct sequence of the Cr, Si and Au layers is as stated in this present paper.)

Wolf ED. (1974). Micrographs of insulated gate field-effect transistor and failed aluminum conductor published as Figs. 6.17(a) thru (d) in Scanning Electron Microscopy, O.C. Wells, A. Boyde, E. Lifshin, A. Rezanowich , McGraw Hill, NY, p. 128.

Wolf ED and Everhart TE. (1969a). Annular diode detector for high angular resolution pseudo-Kikuchi patterns, Scanning Electron Microsc. 1969; 41-44.

Wolf ED and Everhart TE. (1969b). Electron beam channeling in single crystal silicon by scanning electron microscopy. Appl. Phys. Lett., **14**, 299-300.